JOURNAL OF COMPUTATIONAL PHYSICS **123,** 476–494 (1996)
ARTICLE NO. 0038

A Moving Spectral Element Approach to the Dynamically Loaded Journal Bearing Problem

D. RH. GWYNLLYW, A. R. DAVIES, AND T. N. PHILLIPS

Department of Mathematics, University of Wales, Aberystwyth SY23 3BZ, United Kingdom

Received January 3, 1995; revised June 6, 1995

A moving spectral element method is described for solving the dynamically loaded journal bearing problem. The journal bearing geometry comprises two eccentric cylinders with a lubricant occupying the region between them. The inner cylinder (the journal) rotates and is also free to move under a time-dependent load, while the outer cylinder (the bearing) is stationary. Lubrication engineers are interested in the dependence of the minimum oil film thickness on viscosity and viscoelasticity. The numerical method is validated by comparing the paths with those generated from lubrication theory. A study of the effect the choice of cavitation model has upon the journal's locus is made and is found to be critical. The possibility of an improved cavitation model is discussed.

1. INTRODUCTION

The traditional approach to the study of journal bearing lubrication has been via the "*lubrication approximation*" introduced by Reynolds [15]. This enables an equation for the pressure within the thin film region of the geometry (the Reynolds equation) to be written separately from the kinematical and constitutive equations describing the flow of the lubricant, thereby simplifying greatly the calculation of the reaction forces engendered by the lubricant. Whereas the effectiveness of the lubrication approximation has been supported by experimental evidence in a very wide range of lubrication studies, there are at least two contexts in which the approximation may be open to question. The first is in predicting the fine details of the nonlinear dynamics of the journal bearing. Here the precise pressure boundary conditions exploited in the Reynolds equation can have a profound effect on the nonlinear dynamics of the journal [5]. The second context is in studying the role of viscoelasticity in journal bearing lubrication. Within the lubrication approximation, normal stresses are viscosity dominated, making it difficult to accommodate elastic effects in the analysis. However, when the relaxation time of a viscoelastic lubricant is sufficiently high, for example, due to pressure thickening, enhanced normal stresses are possible when the lubrication approximation is not employed [16, 7].

If the lubrication approximation is not invoked, there is no option but to solve the full set of coupled equations (kinematic and constitutive) governing the flow of the lubricant, taking proper account of the moving parts of the geometry. Until recently this task has proved too formidable a calculation, but with current computing power, combined with efficient and accurate numerical methods, the calculation may be attempted. This is the subject the paper addresses.

The complexity of the dynamically loaded journal bearing problem is only too evident if one considers a lubricant in the three-dimensional region between two eccentric cylinders, where the inner cylinder (the journal) rotates and is also free to move under a time dependent load, while the outer cylinder (the bearing) is stationary. This situation models the *main* bearing in car engines as opposed to the *big-end* bearing, whereby it is the outer cylinder that is free to move. We reiterate the more important criteria which must be considered in modelling the behaviour of the lubricant and the nonlinear dynamics of the motion of the journal. These are: incompressibility; the changes in lubricant viscosity with rate of strain, pressure, and temperature; viscoelasticity, also a function of the three previous variables; oil feed; the possible onset of boundary lubrication to accommodate extreme effects when the cylinders are almost touching; heat transfer; and cavitation. Our eventual aim is to study computationally the combined effects of these phenomena on minimum oil film thickness, load-bearing capacity, and bearing dynamics, without invoking the lubrication approximation. The first step, however, is to provide an efficient and accurate computational algorithm which can simulate both the journal and lubricant dynamics.

In this first paper, therefore, the main emphasis must be that of validation of the numerical algorithm. In this respect it is essential to avoid too much complexity in the modelling. We therefore choose to ignore elastic deformation of the bearing, and lubricant viscoelasticity, so that we can meaningfully validate our results against those of basic lubrication theory in contexts where the lubrication approximation is not in serious doubt. We make further

0021-9991/96 $18.00

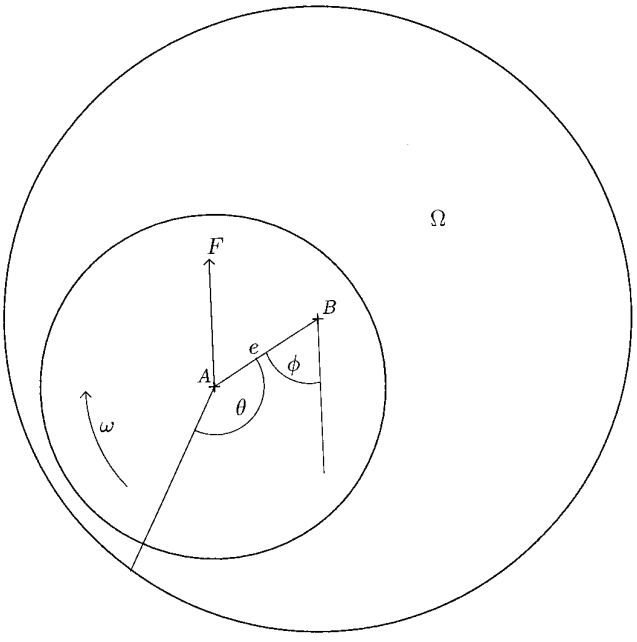

FIG. 1. Schematic diagram of the dynamically loaded journal bearing model.

simplifications by considering infinitely long cylinders (two space dimensions); oil feed may then be justifiably omitted. Although the code is written to treat variable viscosity lubricants, using the inelastic model studied by Davies and Li [7] in another context, in this paper we shall report only the case of isothermal constant viscosity lubricants, again to facilitate easier validation of the algorithm.

2. FORMULATION OF THE PROBLEM

Consider the two-dimensional geometry shown schematically in Fig. 1. The journal of radius R_J rotates with a constant angular velocity ω in a stationary bearing of radius R_B. Both the journal and the bearing are assumed to be of infinite extent in the axial z-direction. The distance between the axes of the journal and the bearing is given by e. The eccentricity ratio is defined by $\varepsilon = e/c$, where $c = R_B - R_J$ is the average gap so that $0 \le \varepsilon \le 1$. The region between the journal and the bearing is occupied by a lubricant. The journal is free to move under the action of an applied load (which may be variable), its own weight, and the reaction force exerted on it by the lubricant. This means that the centre of the journal traces out a nontrivial path in space.

The governing equations for an incompressible inelastic fluid comprise the conservation of momentum

$$\rho\left(\frac{\partial \mathbf{v}}{\partial t} + \mathbf{v}\cdot\nabla\mathbf{v}\right) = -\nabla p + \nabla\cdot\mathbf{T}, \tag{1}$$

the conservation of mass

$$\nabla\cdot\mathbf{v} = 0, \tag{2}$$

and the constitutive equation

$$\mathbf{T} = 2\eta(\dot\gamma, p)\mathbf{d}, \tag{3}$$

where ρ is the density, η is the variable viscosity, $\dot\gamma = \sqrt{2\,\mathrm{tr}(\mathbf{d}^2)}$, $\mathbf{T}$ is the extra-stress tensor, and $\mathbf{d} = \frac{1}{2}(\nabla\mathbf{v} + (\nabla\mathbf{v})^{\mathrm{T}})$ is the rate of deformation tensor. Here $\mathrm{tr}(\mathbf{A})$ denotes the trace of a tensor $\mathbf{A}$. The constitutive equation (3) is a modification of the usual generalised Newtonian model to include pressure dependence of the viscosity.

The viscosity law that we have used was proposed by Davies and Li [7]. It is shear-thinning and pressure-thickening. The various parameters in the model are determined empirically. The dependene of viscosity on $\dot\gamma$ and pressure is given by

$$\eta = \left\{\eta_\infty + \frac{(\eta_0 - \eta_\infty)}{[1 + (\kappa\dot\gamma)^m]}\right\} \times \exp(-\alpha\,\mathrm{tr}(\boldsymbol\sigma)/3 + F), \tag{4}$$

where κ is a function of pressure,

$$\kappa = \kappa(p) = \exp(-\bar\alpha\,\mathrm{tr}(\boldsymbol\sigma)/3 + E),$$

$\boldsymbol\sigma = -p\mathbf{I} + \mathbf{T}$ is the Cauchy stress tensor, and η_0, η_∞, m, n, α, $\bar\alpha$, E, and F are material parameters. This model describes the shear-thinning behaviour of the viscosity by a Cross-type formula. Pressure-thickening is modelled by a simple exponential law [1]. It is important to note that the viscosity law (4) is consistent with experiments [2] which span only limited ranges of the pressures which the lubricants experience under general operating conditions.

The governing equations (1)–(2) are solved subject to specified boundary and initial conditions. These are, respectively,

$$\mathbf{v}(t) = \mathbf{V}_J \quad \text{on } \Gamma_J, \quad \mathbf{v}(t) = \mathbf{0} \quad \text{on } \Gamma_B, \tag{5}$$

$$\mathbf{v}(\mathbf{x}, t = 0) = \mathbf{v}_0(\mathbf{x}), \tag{6}$$

where Γ_J and Γ_B denote the boundaries of the journal and bearing, respectively.

3. THE MOVING SPECTRAL ELEMENT (MSE) METHOD

3.1. Temporal Discretisation

We begin by describing the way in which the governing equations for the fluid are discretised in time. A backward

Euler scheme is used for the temporal discretisation of the momentum equation:

$$\frac{\rho}{\Delta t}(\mathbf{v}^{n+1} - \mathbf{v}^n) = -\nabla p^{n+1} + 2\nabla \cdot \eta \mathbf{d}^{n+1}, \tag{7}$$

$$\nabla \cdot \mathbf{v}^{n+1} = 0. \tag{8}$$

This scheme requires the inversion of an unsteady Stokes operator at each time step subject to velocity boundary conditions on the journal and the bearing (5). In this scheme the velocity and pressure variables at time step $(n + 1)\Delta t$ are coupled. They are decoupled by means of an Uzawa method which we describe later. When the equations are discretised in space a nested solver is required to solve this system. The inversion of the discrete unsteady Stokes operator is the computationally intensive part of the algorithm.

3.2. *Spatial Discretisation*

The spectral element method is based on a weak formulation of the problem. The variational formulation of (7)–(8) is, therefore: Find $(\mathbf{v}, p) \in X \times L_0^2(\Omega)$, such that

$$\begin{aligned} &\iint_\Omega (\eta(\nabla \mathbf{v})^{\mathrm{T}} : \nabla \mathbf{w})\, d\mathbf{x} \\ &\quad + \frac{\rho}{\Delta t}\iint_\Omega (\mathbf{w} \cdot \mathbf{v})\, d\mathbf{x} \\ &\quad - \iint_\Omega (p \nabla \cdot \mathbf{w})\, d\mathbf{x} \\ &\quad = \iint_\Omega (\mathbf{w} \cdot \mathbf{f})\, d\mathbf{x}, \quad \forall\, \mathbf{w} \in X, \end{aligned} \tag{9}$$

$$\iint_\Omega (\nabla \cdot \mathbf{v} q)\, d\mathbf{x} = 0, \quad \forall\, q \in L^2(\Omega), \tag{10}$$

where we have dropped the time level $n + 1$ from the superscript on $\mathbf{v}$ and p. Here $\mathbf{f} = \rho \mathbf{v}^n/(\Delta t)$, $X = H^1(\Omega) \times H^1(\Omega)$, and

$$L_0^2(\Omega) = \left\{ \phi \in L^2(\Omega) : \iint_\Omega \phi = 0 \right\}.$$

The spectral element method is a technique for solving problems defined in complex geometries. The idea is to divide the flow into several spectral elements, Ω_k, $1 \le k \le K$, such that $\bigcup_{k=1}^K \overline{\Omega}_k = \overline{\Omega}$ and $\Omega_k \cap \Omega_l = \varnothing$ for all $k \ne l$. We also assume that the decomposition is geometrically conforming in the sense that the intersection of two adjacent elements is either a common vertex or an entire edge. Each of the spectral elements is mapped onto the parent element $D = [-1, 1] \times [-1, 1]$ using the transfinite mapping technique of Gordon and Hall [8].

With this decomposition of Ω the variational formulation of (7)–(8) may be written in the equivalent form: Find $(\mathbf{v}, p) \in X \times M$, such that

$$\begin{aligned} &\sum_{k=1}^K \left\{ \iint_{\Omega_k} (\eta(\nabla \mathbf{v})^{\mathrm{T}} : \nabla \mathbf{w})\, d\mathbf{x} \right. \\ &\qquad \left. + \frac{\rho}{\Delta t}\iint_{\Omega_k} (\mathbf{w}\mathbf{v})\, d\mathbf{x} - \iint_{\Omega_k} (p \nabla \cdot \mathbf{w})\, d\mathbf{x} \right\} \\ &\quad = \sum_{k=1}^K \iint_{\Omega_k} (\mathbf{w}\mathbf{f})\, d\mathbf{x}, \quad \forall\, \mathbf{v} \in X, \end{aligned} \tag{11}$$

$$\sum_{k=1}^K \iint_{\Omega_k} (\nabla \cdot \mathbf{v} q)\, d\mathbf{x} = 0, \quad \forall q \in L^2(\Omega). \tag{12}$$

The bilinear form a^k is defined by

$$a^k(\mathbf{v}, \mathbf{w}) = \iint_{\Omega_k} \eta(\nabla \mathbf{v})^{\mathrm{T}} : \nabla \mathbf{w}\, d\mathbf{x}. \tag{13}$$

Each element Ω_k is mapped onto the parent element $[-1, 1] \times [-1, 1]$. In this way we may associate with each point $(\xi, \zeta) \in D$ a point $(x(\xi, \zeta), y(\xi, \zeta)) \in \Omega_k$. Under this mapping the expression defining $a^k(\cdot, \cdot)$ becomes

$$\begin{aligned} &a^k(\mathbf{v}, \mathbf{w}) \\ &\quad = \iint_D \frac{\eta}{J^k} \left\{ G_1^k \frac{\partial \mathbf{v}}{\partial \xi}\frac{\partial \mathbf{w}}{\partial \xi} + G_2^k \frac{\partial \mathbf{v}}{\partial \zeta}\frac{\partial \mathbf{w}}{\partial \zeta} \right. \\ &\qquad \left. + G_3^k \left(\frac{\partial \mathbf{v}}{\partial \xi}\frac{\partial \mathbf{w}}{\partial \zeta} + \frac{\partial \mathbf{v}}{\partial \zeta}\frac{\partial \mathbf{w}}{\partial \xi} \right) \right\} d\xi\, d\zeta, \end{aligned} \tag{14}$$

where the Jacobian J^k of the mapping is defined by

$$J^k = \frac{\partial x}{\partial \xi}\frac{\partial y}{\partial \zeta} - \frac{\partial x}{\partial \zeta}\frac{\partial y}{\partial \xi}, \tag{15}$$

$$G_1 = \left(\frac{\partial x}{\partial \xi}\right)^2 + \left(\frac{\partial y}{\partial \xi}\right)^2, \tag{16}$$

$$G_2 = \left(\frac{\partial x}{\partial \zeta}\right)^2 + \left(\frac{\partial y}{\partial \zeta}\right)^2, \tag{17}$$

$$G_3 = -\left(\frac{\partial x}{\partial \xi}\frac{\partial x}{\partial \zeta} + \frac{\partial y}{\partial \xi}\frac{\partial y}{\partial \zeta} \right). \tag{18}$$

We now describe how we set up the corresponding discrete variational problem. Here we approximate the primitive variables using Legendre Lagrangian interpolants of

degree N in both spatial directions. Let $P_{N,K}$ denote the space of polynomials of degree N or less, defined over the K elements. We choose the velocity field in $P_{N,K}$ and construct a Gauss–Lobatto Legendre grid in each of the elements Ω_k, $1 \le k \le K$. The velocity representation is then given by

$$\mathbf{v}_N^k(\xi, \zeta) = \sum_{i=0}^{N} \sum_{j=0}^{N} \mathbf{v}_{i,j}^k h_i(\xi) h_j(\zeta), \tag{19}$$

The Lagrangian interpolants h_i are defined on the parent interval with $\xi \in [-1, 1]$ by the relationship

$$h_i(\xi) = -\frac{(1-\xi^2)L_N'(\xi)}{N(N+1)L_N(\xi_i)(\xi - \xi_i)}, \tag{20}$$

where the points ξ_i are the collocation points on the Gauss–Lobatto Legendre grid. These interpolants satisfy the property

$$h_i(\xi_j) = \delta_{i,j}, \quad 0 \le i, j \le N. \tag{21}$$

As for the finite element method, the velocity and pressure approximations must satisfy the Babuska–Brezzi condition to avoid the presence of spurious modes. In the framework of the spectral element method Maday and Patera [13] have shown that a suitable choice for the pressure approximation space is

$$M_N = L^2(\Omega) \cap P_{N-2,K}. \tag{22}$$

Therefore we choose the pressure nodes to be the interior Gauss–Lobatto Legendre points. Thus the pressure approximation is given by

$$p_N^k(\xi, \zeta) = \sum_{i=1}^{N-1} \sum_{j=1}^{N-1} p_{i,j}^k \hat{h}_i(\xi) \hat{h}_j(\zeta), \tag{23}$$

where $\hat{h}_i(\xi)$ is defined by

$$\hat{h}_i(\xi) = -\frac{(1-\xi_i^2)L_N'(\xi)}{N(N+1)L_N(\xi_i)(\xi - \xi_i)}. \tag{24}$$

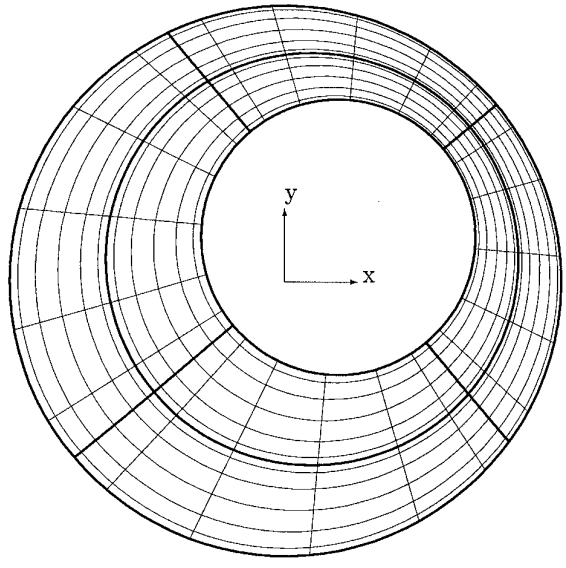

FIG. 2. The discretisation of the physical fluid domain for four elements in the azimuthal direction ($E_a = 4$) and two elements in the radial direction ($E_r = 2$). Each element is split into seven nodes in each direction ($N_r = N_a = 7$).

The spectral element discretisation of the geometry is shown in Fig. 2.

The integrals over each element Ω_k in (11) are approximated by a Gauss–Legendre quadrature rule. The discrete bilinear form a_N^k is therefore written in terms of Gauss–Lobatto Legendre quadrature rule

$$\begin{aligned} a_N^k(\mathbf{v}_N, \mathbf{w}_N) &= \sum_{\mathrm{GL}} \frac{\eta}{J^k} \left[G_1^k \frac{\partial \mathbf{v}_N}{\partial \xi} \frac{\partial \mathbf{w}_N}{\partial \xi} + G_2^k \frac{\partial \mathbf{v}_N}{\partial \zeta} \frac{\partial \mathbf{w}_N}{\partial \zeta} \right. \\ &\quad \left. + G_3^k \left(\frac{\partial \mathbf{v}_N}{\partial \xi} \frac{\partial \mathbf{w}_N}{\partial \zeta} + \frac{\partial \mathbf{v}_N}{\partial \zeta} \frac{\partial \mathbf{w}_N}{\partial \xi} \right) \right], \end{aligned} \tag{25}$$

where Σ_{GL} indicates the sum over all Gauss–Lobatto points in both directions. The velocity and pressure expansions are now inserted into (9)–(10) and the discrete equations are generated by choosing appropriate test functions $\mathbf{w} \in P_{N,K} \cap H_0^1(\Omega)$ which are unity at a single point (ξ_k, ζ_l) and zero at all other Gauss–Lobatto Legendre points and test functions $q \in P_{N-2,K}$ which are unity at a single point (ξ_k, ζ_l) and zero at all other interior Gauss–Lobatto Legendre points. Once the discrete bilinear forms have been computed for all elements, the contributions from neighbouring elements are summed along element interfaces. This procedure takes into account the situations in which the test function extends into more than one element. In this way we obtain the system of algebraic equations

$$A\mathbf{v} + \sigma B\mathbf{v} - D^{\mathrm{T}}\mathbf{p} = \mathbf{g}, \tag{26}$$

$$D\mathbf{v} = \mathbf{h}, \tag{27}$$

where D is the discrete divergence operator, its transpose is the discrete gradient operator, B is the mass matrix, and $\sigma = \rho/\Delta t$. The vectors $\mathbf{g}$ and $\mathbf{h}$ derive from the right-hand side of Eqs. (9) and (10) and also from the velocity boundary conditions (5). The vectors of unknowns now refer to their values at the discretisation points (the Gauss–Lobatto nodes). Note that in order to evaluate the discrete gradient and divergence operators we need to map the pressure p_N and the test function q_N within each spectral element from the interior Gauss–Lobatto Legendre nodes onto the Gauss–Lobatto Legendre nodes on the boundary of the element.

Block Gaussian elimination yields a symmetric semi-positive definite system for the pressure unknowns

$$S\mathbf{p} = \mathbf{c}, \tag{28}$$

where $S = D(A + \sigma B)^{-1} D^{\mathrm{T}}$ and $\mathbf{c} = -D(A + \sigma B)^{-1}\mathbf{f} + \mathbf{g}$. The matrix S is made positive definite by imposing a zero volume condition on the pressure field to eliminate its arbitrariness. The velocity is computed using

$$(A + \sigma B)\mathbf{v} = D^{\mathrm{T}}\mathbf{p} + \mathbf{f}. \tag{29}$$

Due to the properties of S, and its considerable size, an iterative solver for (28) is required. It can be shown that the maximum eigenvalue of S is fixed and is of order unity while the minimum eigenvalue scales like β_N^{-2}, where β_N is the lower bound of the discrete inf–sup condition. Hence there is a necessity from the solution point of view to have a good inf–sup condition. Using the preconditioned conjugate gradient (PCG) method to solve this system is well documented [12] and using a suitable preconditioner the PCG method is found to be very efficient. For the journal bearing geometry the high physical aspect ratios encountered in practice mean that the standard choice of preconditioner for the Stokes problem, i.e., the pressure mass matrix, is not robust. Further details regarding the choice of preconditioners for these sorts of systems can be found in [9]. The iterative scheme is nested since each matrix–vector multiplication $S\mathbf{p}$ requires the solution of the system

$$(A + \sigma B)\mathbf{r} = \mathbf{s}. \tag{30}$$

This system is also solved by the PCG method since it is a symmetric positive definite system.

3.3. Uzawa Algorithm

For the unsteady Stokes problem the resulting pressure matrix, S, is given by

$$S = D(A + \sigma B)^{-1} D^{\mathrm{T}}, \tag{31}$$

with, again, $\sigma = \rho/\Delta t$. In the steady problem the pressure matrix is naturally well-conditioned. This is not the case in the corresponding unsteady problem [9].

We propose using a preconditioner which changes dynamically in time, taking into account the current eccentricity ratio of the journal and the number of PCG iterations required for convergence at each time step. The preconditioner is based on the pressure matrix evaluated at a given eccentricity ratio. This preconditioner is used for the solution of the pressure problem at successive time steps for which, of course, the eccentricity ratio will be different from that of the preconditioner. The current preconditioner is changed when the number of iterations required for convergence of the outer conjugate gradient iteration exceeds a prescribed maximum number of iterations. In the results which we present this was set at 12. A new preconditioner is then constructed corresponding to the current eccentricity ratio. This process continues until either the bearing fails or a stable equilibrium point or closed orbit is found.

3.4. Motion of the Journal

We assume that the centre of mass of the journal behaves as a particle of effective mass, M_e, situated at the centre of the journal. The equation of motion of the journal is then given by

$$M_e\ddot{\mathbf{r}} = \mathbf{F} + \mathbf{R}, \tag{32}$$

where $\mathbf{r}$ is the position vector of the centre of the journal with respect to a coordinate system fixed in space. $\mathbf{F}$ is the applied load, which, in this paper, is taken to be

$$\mathbf{F} = (0, F), \quad F = F_p \sin(\omega t) - M_e g + F_c, \tag{33}$$

where the parameters F_p and F_c allow one to specify the amplitude and mean level of the applied load. $\mathbf{R}$ is the reaction force which the fluid exerts on the journal. $\mathbf{R}$ is determined from the solution of the governing equations of motion for the lubricant.

The journal is tracked in time using (32) by using one of two methods. The first method is based on a quasi-steady approximation. At a given time $t = n\Delta t$, say, the steady flow equations are solved for the current position of the journal using the spectral element method. Since the mesh in this approach is generated afresh at each time step we do not have to take into account the speed of

change of the mesh in the governing equations. The force which the fluid exerts on the journal is then calculated by integrating the normal stress around the journal. The right-hand side of (32) is then updated and the equation is integrated in time using the forward Euler method to obtain the new position of the journal at time $t = (n + 1)\Delta t$. The process is repeated by solving the steady flow equations in the new region between the journal and the bearing. Note that in this approximation the solutions to the fluid equations at successive time steps are independent of one another.

The second method shifts the values of the variables between spectral element meshes at two successive time steps, provided the maximum translation of the mesh points is small. We have termed this process "non-interpolating spatial discretisation with adaptive time-stepping"—an obvious acronym for which is NISDAT. To perform the dynamic remeshing exactly would involve the Lagrangian interpolation of high order polynomials at some $O(N^2)$ nodes at each time step. This task involves two steps: first, determination of the new nodal positions under translational motion of the bearing in time Δt; second, interpolation of the previous field values on the new mesh. It is the second step which is the more time consuming (by orders of magnitude). If Δt is made sufficiently small, however, the error incurred by simply carrying the old field values onto the new mesh *without interpolating* can be kept to $O(\Delta t)$. This means that the overall accuracy is kept to $O(\Delta t)$. The time step Δt can be chosen adaptively as follows.

We denote the number of spectral elements in the radial and azimuthal directions by E_r, E_a, respectively and, similarly, $N_r + 1, N_a + 1$ denote the number of Gauss–Lobatto nodes in those respective directions (see Fig. 2). The minimum internodal distance is then

$$h_{\min} \approx \frac{c}{E_r N_r^2}.$$

If U_T denotes the translational speed of the journal, then the distance moved in time Δt is

$$h \approx U_T \Delta t.$$

The error incurred by not interpolating is negligible if $h \ll h_{\min}$, i.e.,

$$\Delta t \ll \frac{c}{E_r N_r^2 U_T}.$$

Now in a typical run, $E_r N_r^2 U_T = O(1)$, while $c = O(10^{-6})$, giving $\Delta t \ll 10^{-6}$. This is well within the feasibility limit of $\Delta t = 10^{-9}$ which we have used.

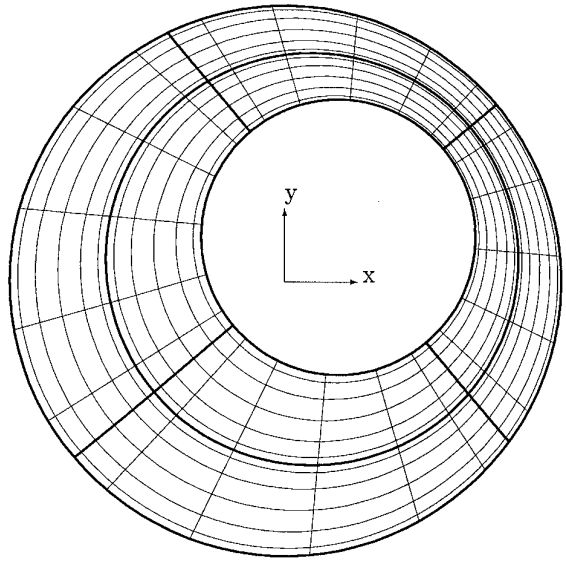

FIG. 2. The discretisation of the physical fluid domain for four elements in the azimuthal direction ($E_a = 4$) and two elements in the radial direction ($E_r = 2$). Each element is split into seven nodes in each direction ($N_r = N_a = 7$).

In this paper we restrict attention to the creeping flow of Newtonian lubricants. We have found that the paths obtained for the centre of the journal, under identical operating conditions, using the NISDAT algorithm or the quasi-steady algorithm are almost indistinguishable. We attribute this to the absence of inertia and viscoelasticity. The quasi-steady algorithm is less demanding of processing time and is therefore preferable for Newtonian lubricants in the absence of inertia.

4. VALIDATION OF THE MSE METHOD

In this section we validate our quasi-steady algorithm in situations where the lubrication approximation is not in serious doubt. In particular, we confirm that results from the moving spectral element code agree with standard results for (i) the statically loaded journal bearing problem (by switching off the journal dynamics), (ii) the journal subjected to an instantaneous squeeze velocity, and (iii) the constant load predictions of Brindley *et al.* [3].

4.1. Validation of the Spatial Discretisation

In this subsection we will deal only with a noncavitating fluid, that is the region between the journal and the bearing is permanently filled with oil. Two examples are given for which lubrication theory furnishes closed form expressions for the reaction force the fluid exerts on the journal.

The spatial accuracy of the spectral element method is analysed by varying the number of elements and the degree

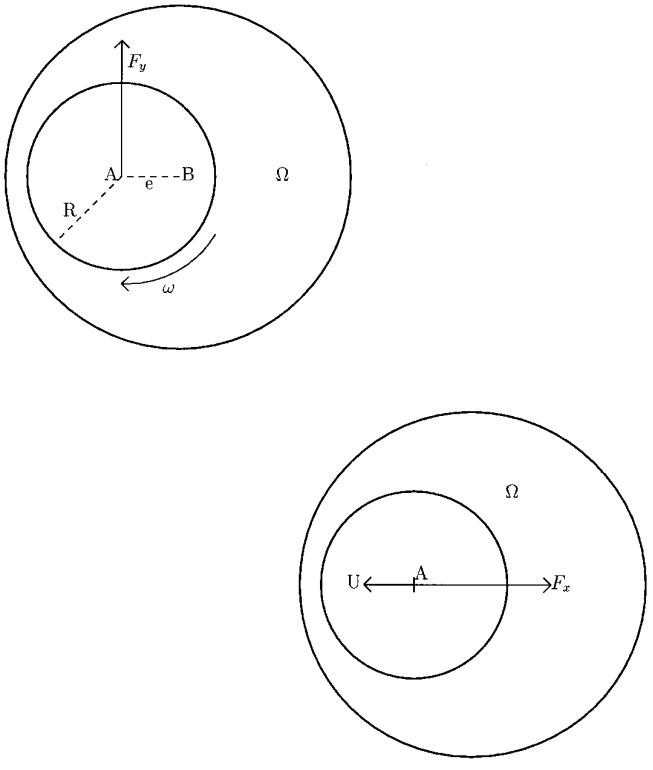

FIG. 3. Schematic diagram of the journal bearing model with a full-film Newtonian fluid incorporating (a) statically loaded with angular velocity ω, (b) instantaneous squeeze film velocity.

of the spectral approximations within each element and comparing with the reaction force derived from lubrication theory.

Statically Loaded Journal Bearing

In this problem the journal rotates with an angluar velocity ω about its own axis but is not allowed to move translationally. The load on the journal acts perpendicular to the line joining the centres of the journal and the bearing. This situation is illustrated in Fig. 3a. Lubrication theory, [6], gives

$$R_y = 12\pi\eta\omega \frac{R^3}{c^2} \frac{\varepsilon}{(2+\varepsilon^2)(1-\varepsilon^2)^{1/2}}, \tag{34}$$

where R_y is the reaction force per unit length (two-dimensional force) that the fluid applies to the journal in the vertical direction.

Journal Subjected to an Instantaneous Squeeze Velocity

In this problem the journal has imparted upon it a constant squeeze velocity U along the line joining the centres of the journal and the bearing and towards the bearing. In this case the load on the journal acts along this line and away from the bearing. This situation is illustrated in Fig. 3b. Lubrication theory, [6], gives the following closed-form expression for the reaction force per unit length on the journal in the horizontal direction

$$R_x = 12\pi\eta U \frac{R^3}{c^2} \frac{1}{(1-\varepsilon^2)^{3/2}}. \tag{35}$$

Numerical Results

The reaction force of the fluid on the journal is calculated by

$$\mathbf{R} = -\int_{\Gamma_J} \boldsymbol{\sigma}\cdot\hat{\mathbf{n}}\, ds, \tag{36}$$

where Γ_J is the journal's surface, $\boldsymbol{\sigma} = -p\mathbf{I} + \mathbf{T}$ is the Cauchy stress tensor, and $\hat{\mathbf{n}}$ is the outward unit normal vector on the journal.

In Tables I and II we compare the forces predicted by lubrication theory with those calculated using our spectral element algorithm for different spatial discretisations for a range of eccentricity ratios. The relative percentage difference between the numerically calculated forces and those given in (34), (35) are shown in these tables. Generally speaking, as the spectral element mesh is refined, better agreement is obtained with the lubrication theory results. Furthermore, the discretisations with $(E_r, E_a) = (4, 1)$ are in better agreement than $(E_r, E_a) = (2, 2)$. This is not surprising since lubrication theory assumes no variation of pressure in the radial direction and, therefore, a finer spatial discretisation in this direction is to be expected for the accurate resolution of the corresponding fully nonlinear problem. The construction of the bearing shells means that the roughness of the surface can give rise to surface variations up to 2% of the average gap c and so for $\varepsilon > 0.98$ we reach physically unrealistic operating conditions for the journal bearing.

4.2. Validation of the Transient Scheme

A single computer run tracking the bearing from rest to a periodic equilibrium state takes many hours of DEC alpha CPU time, under realistic running conditions. Two factors are primarily responsible for the high CPU time. These are the use of small time steps which are required for stability and accuracy, typically $O(10^{-8})$, and the dynamic remeshing due to the translational motion of the journal.

Brindley *et al.* [3] have modelled the dynamic behaviour of the journal bearing when it moves, subject to a constant load which is its own weight, using the lubrication approximation. We shall validate our quasi-steady moving spectral element algorithm by comparing the results from this algorithm with those from Brindley *et al.*'s equations, under

TABLE I

Comparison between Lubrication Theory and Spectral Element Method for the Model Illustrated in Fig. 3a

	F_y	Relative difference in percentages				
ε	Lub. theory	(8, 8, 2, 2)	(14, 14, 2, 2)	(8, 8, 1, 4)	(11, 11, 1, 4)	(14, 14, 1, 4)
0.1	4.4971×10^4	0.06	0.06	0.06	0.06	0.06
0.3	1.3525×10^5	0.06	0.06	0.06	0.06	0.06
0.5	2.3064×10^5	0.02	0.06	0.06	0.06	0.06
0.6	2.8564×10^5	0.04	0.06	0.06	0.06	0.06
0.7	3.5382×10^5	0.05	0.06	0.06	0.06	0.06
0.75	3.9772×10^5	0.01	0.06	0.04	0.06	0.06
0.8	4.5395×10^5	0.05	0.06	0.00	0.06	0.06
0.85	5.3271×10^5	0.62	0.06	0.06	0.06	0.06
0.9	6.6044×10^5	3.10	0.03	0.06	0.06	0.06
0.95	9.4215×10^5	9.59	0.08	1.52	0.09	0.06
0.96	1.0548×10^6	10.6	0.04	3.29	0.11	0.05
0.97	1.2195×10^6	10.3	0.02	0.07	0.11	0.00
0.98	1.4952×10^6	7.93	0.96	11.3	0.72	0.12

identical operating conditions of the journal bearing. We recall that the difference between our approach and that of Brindley *et al.* is that we do not invoke the lubrication approximation and we solve, instead, the full set of governing equations for the lubricant.

We consider three different scenarios, distinguished by their approach to cavitation modelling:

(1) No cavitation.

(2a) Single phase π-film cavitation.

(2b) Dual phase π-film cavitation.

(3) Single phase variable-film cavitation.

Each approach is defined in the appropriate section following.

4.2.1. *Absence of Cavitation*

Many investigators [11, 14] suggest that, in the case of an unloaded journal operating under the assumption of full-film conditions, instability is universal. In this case the journal moves from its equilibrium position (under static loading conditions) in an orbit of growing size until the bearing ultimately fails, i.e., the journal and bearing surfaces touch one another. This phenomenon is known as whirl instability. In practice the full-film assumption is not realistic since in many journal-bearing models the large negative pressures produced in the oil cause the oil to vapourise, leading to cavitation.

Brindley *et al.* [3] have studied the nonlinear dynamics of this problem using the Reynolds equation of lubrication theory. We shall review briefly their approach and indicate how it differs from the one we have adopted. In nondimensional form Reynolds' equation assumes the form

$$\frac{\partial}{\partial\theta}\left\{(1+\varepsilon\cos\theta)^3\frac{\partial\bar{p}}{\partial\theta}\right\} + \left(\frac{R_J}{L}\right)^2\frac{\partial}{\partial z}\left\{(1+\varepsilon\cos\theta)^3\frac{\partial\bar{p}}{\partial z}\right\} = \frac{6}{\pi}S\{-\varepsilon(1-2\dot{\phi})\sin\theta + 2\dot{\varepsilon}\cos\theta\}, \tag{37}$$

where the nondimensional parameter S, the Sommerfeld number, is given by

$$S = \frac{R_J^3\eta\omega}{\pi W c^2}, \tag{38}$$

and W is the *effective* weight per unit length of the journal. The angle θ is shown in Fig. 1. The Reynolds equation is solved subject to appropriate boundary conditions for the nondimensional pressure,

$$\bar{p} = \frac{p}{\eta\omega(R_J/c)^2}. \tag{39}$$

The assumption made in deriving the Reynolds equation is that $c/R_J \ll 1$. If the long-bearing approximation is now applied; i.e., if we assume that everything is constant in the z-direction and we impose the boundary conditions

$$p(0) = p(2\pi) = 0,$$

TABLE II

Comparison between Lubrication Theory and Spectral Element Method for the Model Illustrated in Fig. 3b

	F_y	Relative difference in percentages				
ε	Lub. theory	(8, 8, 2, 2)	(14, 14, 2, 2)	(8, 8, 1, 4)	(11, 11, 1, 4)	(14, 14, 1, 4)
0.1	9.1247×10^5	0.19	0.19	0.19	0.19	0.19
0.3	1.0354×10^6	0.18	0.19	0.19	0.19	0.19
0.5	1.3838×10^6	0.16	0.19	0.19	0.19	0.19
0.6	1.7555×10^6	0.01	0.19	0.19	0.19	0.19
0.7	2.4678×10^6	0.78	0.19	0.18	0.19	0.19
0.75	3.1060×10^6	1.58	0.19	0.18	0.19	0.19
0.8	4.1612×10^6	2.51	0.18	0.18	0.19	0.19
0.85	6.1486×10^6	2.87	0.17	0.09	0.19	0.19
0.9	1.0853×10^7	3.12	0.16	0.75	0.17	0.20
0.95	2.9523×10^7	21.7	1.58	3.66	0.08	0.18
0.96	4.0945×10^7	33.0	3.09	3.78	0.26	0.16
0.97	6.2559×10^7	48.1	4.84	3.56	1.32	0.16
0.98	1.1406×10^8	66.5	4.79	6.87	3.59	0.01

we may obtain an explicit expression for the pressure. The pressure is then integrated around the surface of the journal to obtain the reaction force of the fluid on the journal:

$$\mathbf{R} = \int_{\Gamma_J} p\mathbf{I} \cdot \hat{\mathbf{n}}\, ds. \tag{40}$$

Note that this expression differs from the one which we use (Eq. (36)) in that the extra-stress part of the Cauchy stress tensor is not included. The expressions for the components of the reaction force are then inserted into the equation of motion of the journal and the nonlinear dynamics of the resulting differential system are studied by computing solutions to these equations.

The result of this investigation by Brindley and co-workers is that under full-film conditions every trajectory spirals towards the bearing and no stable equilibrium points or closed orbits are found for any of the parameters tested. Further, as the journal approaches the bearing the whirl speed approaches half shaft speed—a phenomenon known as half-speed or half-frequency whirl. The mechanism for instability seems to be half-frequency whirl.

Cameron [6] gives an heuristic argument explaining the onset of half-whirl instability. At high eccentricities the journal is travelling in an almost circular path about the centre of the bearing. Using a crude mass balance he shows that the whirl occurs at half-shaft speed; i.e., the frequency of the motion of the journal about the bearing centre is twice the frequency of the rotation of the journal. This is a dangerous situation since the load-bearing capacity of the journal is zero and bearing failure is inevitable.

We apply the moving spectral element algorithm described earlier to the dynamically loaded journal bearing problem under the assumption of full-film conditions using the quasi-steady approximation. The only time dependence in this formulation is due to the motion of the journal. The quasi-steady assumption is also made in the work of Brindley *et al.* [3]. Thus the only difference between the two approaches is due to the lubrication approximation. The values of the physical parameters used in the examples presented in this paper are given in Table III. We have used the numerical parameter values given by $(N_r, N_a, E_r, E_a) = (8, 8, 1, 4)$. When values other than these default values are used it is clearly stated.

We find that the paths generated by the lubrication approximation of [3] and those generated by our quasi-steady algorithm are in visual agreement. Therefore we also predict universal instability for the journal subject to constant load under full-film assumptions. So irrespective of the value of the *effective* mass M_e we do not achieve a global minimum oil film thickness and so the bearing fails. We also observe that as the journal approaches the bearing it exhibits half-frequency whirl. We present three examples illustrating this instability. In each case the initial position of the journal is specified by an initial eccentricity ε_0 and an initial attitude angle ϕ_0. Since, in this paper, we are

TABLE III

The Default Values for the Physical Parameters Used in This Paper

Journal radius (R_J)	0.031250 m
Bearing radius (R_B)	0.031290 m
Constant viscosity (η)	5×10^{-3} Pas
Gravity acc^n (g)	10 m/s^2
Density [NISDAT only] (ρ)	820 kg/m^3

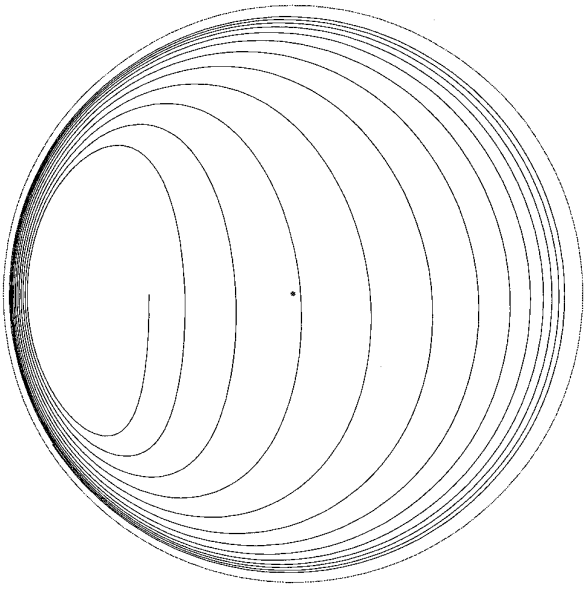

FIG. 4. The path of a journal for full-film condition with $M_e = 5 \times 10^4$ kg/m, $\omega = 250$ rad/s, $(\varepsilon_0, \phi_0) = (0.5, \pi/2)$, time $t \in$ [0s, 0.70s], and constant applied load $M_e g$ ($F_c = F_p = 0$).

dealing with a two-dimensional model any reference to the *effective* mass, M_e, shall be to the effective mass per unit length of the journal.

Figures 4, 5, and 6 correspond to the path, eccentricity, and attitude angle of a journal of effective mass per unit length $M_e = 10^5$ kg/m, with angular velocity $\omega = 250$ rads/s moving from an initial position of $(\varepsilon_0, \phi_0) = (0.5, \pi/2)$. In all figures in this paper, time t is in seconds. The initial downward path is due to the weight of the journal (the constant applied load) but as the eccentricity increases the mechanism generating a half-speed whirl becomes dominant (Fig. 6). Brindley *et al.* in [3] report that the limiting path is indeed a half-speed whirl.

In [3] it is shown that the path of the journal, calculated from the lubrication approximation, is determined by four parameters, namely the two that determine its initial position (ε_0, ϕ_0), the Sommerfeld number given in (38), and a dimensionless angular velocity $\overline{\omega}$ given by

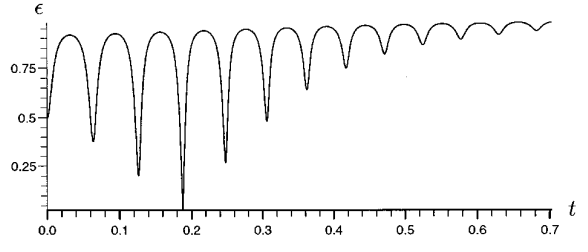

FIG. 5. Plot of the eccentricity of the journal's path shown in Fig. 4.

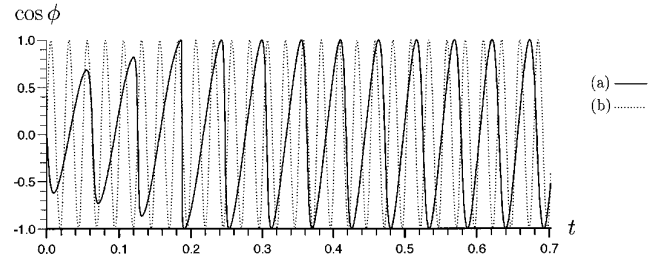

FIG. 6. Plot of (a) the cosine of the attitude angle of the journal path shown in Fig. 4, together with (b) $k_1 + k_2 \sin(\omega t)$ for reference with the journal's angular velocity.

$$\overline{\omega} = \omega(2M_e c/W)^{1/2}. \tag{41}$$

The values of the nondimensionalised parameters for the above example are $(S, \overline{\omega}) = (0.01524, 0.7071)$. However, we note that if gravity is absent, the nondimensionalisation used in [3] is not applicable and the paths generated by journals of differing masses are different, despite the values of S and $\overline{\omega}$ being "constant" at ∞. This is shown below by setting gravity to be zero ($W = 0$), where Figs. 7, 8, and 9 correspond to the path, eccentricity, and attitude angle of a journal of effective mass $M_e = 10^5$ kg/m whilst Figs. 10 and 11 correspond to the eccentricity and attitude angle of journal of effective mass $M_e = 10^3$ kg/m. We shall discuss later in the paper the choice of a realistic value of M_e. Despite having no weight, the trend of these results agree with those of [3] in the sense that the journal of large mass

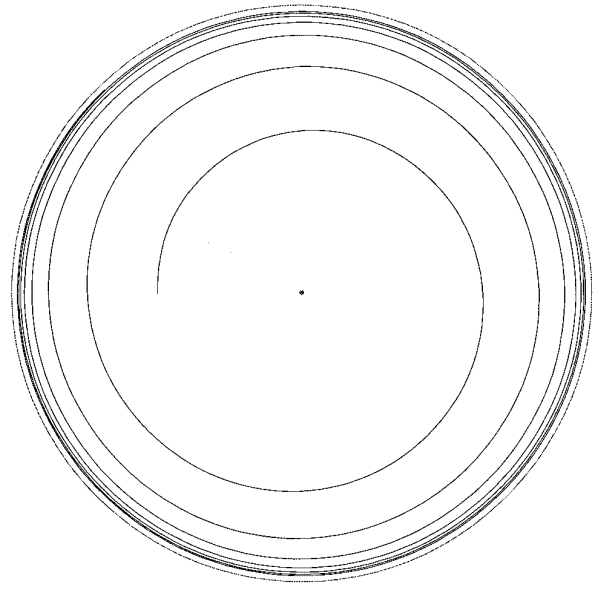

FIG. 7. The path of a journal for full-film condition with $M_e = 1 \times 10^5$ kg/m, $\omega = 250$ rad/s, $(\varepsilon_0, \phi_0) = (0.5, \pi/2)$, time $t \in$ [0s, 0.36s], and zero applied load ($F_c = M_e g$).

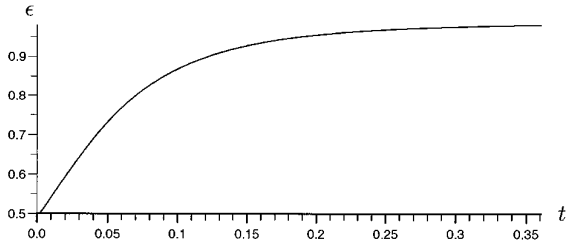

FIG. 8. Plot of the eccentricity of the journal's path shown in Fig. 7.

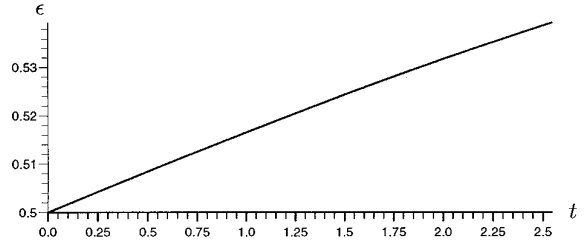

FIG. 10. Plot of the eccentricity of a journal of $M_e = \times 10^3$ kg/m with $\omega = 250$ rad/s and $(\varepsilon_0, \phi_0) = (0.5, \pi/2)$ with time $t \in [0s, 0.25s]$ and zero applied load ($F_c = M_e g$).

has a much greater propensity to spiral outwards than one of less mass, although the path of the low mass journal will still result in bearing failure. The computations were terminated once an eccentricity ratio of 0.98 was reached. The eccentricity ratio versus time graph show that the rate at which the eccentricity increases is small for the smaller mass, although it is monotonic. Both cases will approach half-speed whirl as the eccentricity ratio approaches unity; this is illustrated in the heavier mass case since in Fig. 8 the gradient approaches zero as $\varepsilon \to 1$, and in Fig. 9 the period of the attitude angle is approximately twice that of the angular velocity. In fact, in the seven complete cycles of the heavier mass, the whirl speed on the first cycle is 0.518ω, whilst on the seventh cycle it is within 0.1% of half speed.

4.2.2. *Simple Cavitation Models*

The assumption that a complete lubricating film is maintained throughout the operation of a journal bearing is well known to be false in many realistic situations. Under certain operating conditions the lubricating film ruptures and a cavity is formed. The presence of a cavity can be a stabilising influence on the journal. Brindley *et al.* [3] show that for a cavitated bearing there are regions of the parameter space in which stable trajectories of the journal can be found and that within the same regions, under full-film conditions, the corresponding loaded bearing would be unstable.

The simplest cavitation model is the so-called π-film model which is sometimes referred to as the half-Sommerfeld condition. This model assumes that the cavitated region is the divergent half of the region between the journal and the bearing. The lubricant is assumed to occupy the convergent part of this region. Thus for the purposes of calculating the force exerted on the journal by the fluid we set

$$p = 0 \quad \text{at } \theta = 0; \quad \pi < \theta < 2\pi. \tag{42}$$

A more sophisticated model which can be used if the short bearing approximation is employed is the oscillating π-film model. This allows the cavitated region to change dynamically in response to the dynamical behaviour of the journal. In this model the value of θ_1 is chosen to be the smallest value of $\theta > \pi$ for which $p = 0$ and the cavity is then assumed to occupy the region $\pi + \theta_1 < \theta < 2\pi + \theta_1$.

Brindley *et al.* [3] investigate the stability of the journal bearing system with $F = M_e g$, using the lubrication approximation. A linear analysis of the stability of the equilibrium point (ε_f, ϕ_f) is made with respect to two parameters. These are the Sommerfeld number S and the dimensionless angular velocity $\overline{\omega}$ (see Eqs. (38), (41)). The analysis showed the existence of both stable and unstable trajectories when a cavitation model is included. Increasing either S or $\overline{\omega}$ was found to have a destabilising effect on the

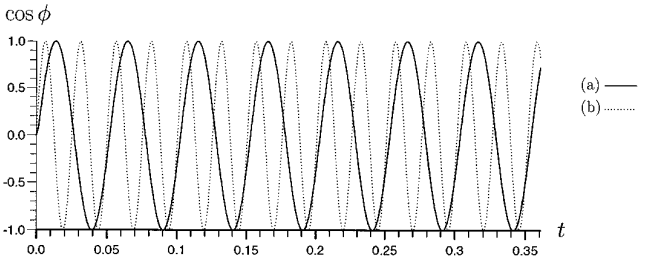

FIG. 9. Plot of (a) the cosine of the attitude angle of the journal path shown in Fig. 7, together with (b) $k_1 + k_2 \sin(\omega t)$ for reference with the journal's angular velocity.

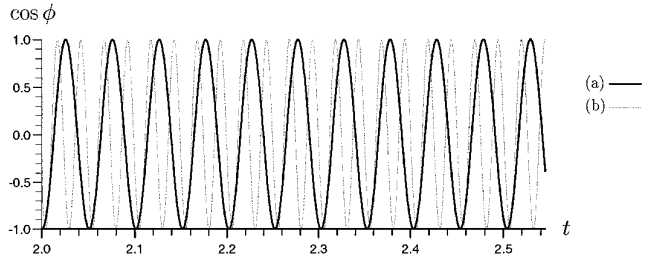

FIG. 11. Plot of (a) the cosine of the attitude angle of the journal path with parameters given in Fig. 10, together with (b) $k_1 + k_2 \sin(\omega t)$ for reference with the journal's angular velocity. Note this graph only shows the times of $t = [2.0, 2.5]$ for reasons of clarity of plot.

trajectories. Regions of the parameter space were found which produced stable equilibrium points, closed orbits, or unstable orbits.

We have incorporated the π-film model into our algorithm to see if cavitation plays as significant a role in the stability of the journal for the full fluid equations as it does in the lubrication approximation. As mentioned earlier, two different cavitation models are used and the differences discussed.

Dual Phase Cavitation Model. Our dual phase cavitation model is the fully nonlinear version of the cavitation model of [3]. Here the quasi-steady algorithm treats the full fluid equations under the assumption of a π-film cavitation model. This is done by setting the viscosity of the fluid in the cavitating region to be very low (ideally, the viscosity of air) whilst keeping the viscosity of the fluid in the non-cavitating region as that of the lubricant. The result of this is that, in our numerics, every element is either full of fluid or fully cavitating. Despite the fact that only the viscosity, and not its gradients, is used in our numerics we would envisage serious numerical difficulties if the viscosity discontinuity did not lie on an elemental interface. We will discuss in the concluding remarks the situation in which the free-surfaces are unknown a priori or do not lie on a convenient straight line.

We can compare our journal paths directly with those generated by Brindley *et al.* [3] by solving the nonlinear differential system

$$\varepsilon'' - \varepsilon\phi'^2 = -24\pi^2 \frac{S}{\overline{\omega}}\left[\frac{\varepsilon'}{(1-\varepsilon^2)^{3/2}}\right] + 2\cos\phi, \qquad (43)$$

$$\varepsilon\phi'' + 2\varepsilon'\phi' = 24\pi^2 \frac{S}{\overline{\omega}}\left[\frac{\varepsilon(\overline{\omega} - 2\phi')}{(2+\varepsilon^2)(1-\varepsilon^2)^{1/2}}\right] - 2\sin\phi, \qquad (44)$$

where the prime denotes differentiation with respect to a dimensionless time T given by

$$T = t(W/2M_e c)^{1/2}.$$

To illustrate the effect that this cavitation model has on the journal's path we use, as our first example, a journal with an angular velocity of $\omega = 884$ rad/s under a constant applied load of just its weight. The result is illustrated in Fig. 12 which shows the comparison of the trajectories of the journal with a full-film and with the *dual-phase* π-film model. In the case of full-film conditions the journal spirals outwards as described earlier. However, when the simple cavitation model is included the journal travels in a decreasing spiral until it reaches an equilibrium point, i.e., the point at which the constant applied load is equal to the force exerted on the journal by the fluid.

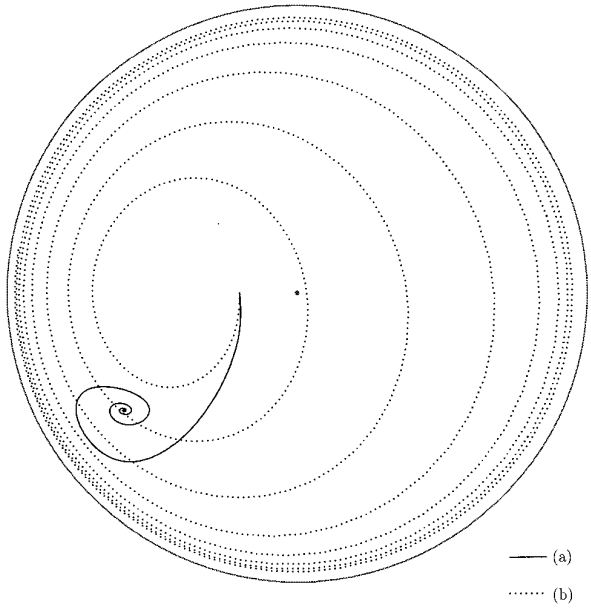

FIG. 12. Comparison of journal path between (a) the dual-phase cavitation model and (b) a full-film model. Physical parameters are $M_e = 4.5 \times 10^4$ kg/m, $\omega = 500$ rad/s, $(\varepsilon_0, \phi_0) = (0.2, \pi/2)$, and constant applied load $M_e g$ ($F_c = F_v = 0$).

As in the full-film case, comparing the paths of our fully nonlinear model and that of the lubrication theory (43), (44) produced no visible difference.

Single Phase Cavitation Model. We call our second cavitation model *single phase cavitation*. In this approach the fluid equations are solved under the assumption of full-film and it is only in the following calculation of the forces that the cavitation model is applied, that is, by integrating over the non-cavitating region. For the purposes of validating the fully nonlinear model with the lubrication approximation we shall deal here with the π-film cavitation. In the next section we describe the variable-film single-phase approach.

The motivation behind this approach was based upon the simplicity of the model and also that for a statically loaded problem the π-film single phase approach is valid. This is due to the anti-symmetry of the pressure field that is generated in the full-film case; the result of this is that in the π-film case for a statically loaded journal the reaction force generated by lubrication theory is the same as that produced when integrating the full-film pressure field over the π-film. As the journal becomes dynamic the anti-symmetry of the pressure field is lost and we are interested in how much difference that makes to the journal's path using *single phase cavitation*.

The result of lubrication theory, by integrating the full-

film pressure field over $[0, \pi]$ and by following closely the approach of [3] gives the following set of coupled ordinary differential equations for the motion of the journal

$$\varepsilon'' - \varepsilon\phi'^2 = -12\pi\frac{S}{\overline{\omega}}\left[\frac{2\varepsilon^2(\overline{\omega} - 2\phi')}{(2+\varepsilon^2)(1-\varepsilon^2)} + \frac{\pi\varepsilon'}{(1-\varepsilon^2)^{3/2}}\right] + 2\cos\phi \quad (45)$$

$$\varepsilon\phi'' + 2\varepsilon'\phi' = 12\pi\frac{S}{\overline{\omega}}\left[\frac{\varepsilon\pi(\overline{\omega} - 2\phi')}{(2+\varepsilon^2)(1-\varepsilon^2)^{1/2}} + \frac{4\varepsilon'}{(1-\varepsilon^2)(1+\varepsilon)}\right] - 2\sin\phi. \quad (46)$$

As in the case of *dual phase cavitation* mentioned earlier, the journal's path, with π-film *single phase cavitation* and lubrication approximation, is uniquely determined by the four parameters, ε_0, ϕ_0, $\overline{\omega}$, and S.

As in the full-film model and *dual-phase cavitation* there is no visual difference to report between the paths from the fully nonlinear model and lubrication theory. Having validated the fully nonlinear model we now proceed to concentrate upon the differences in the paths generated using single-phase cavitation (π-film and variable film) and the π-film dual phase cavitation.

4.2.3. *Single-Phase Variable-Film Cavitation Model*

Before making a comparison between the single- and dual-phase cavitation approaches we need to describe the *variable-film single-phase cavitation model*. This model, as in the π-film model described above, makes the assumption that the pressure on the journal at the point of smallest gap is ambient. However, unlike the π-film approach, no other assumption is made about the size of the cavitating region. The fluid's equations are solved using the single-phase approach and the cavitating region determined by the region of subambient pressures. The reaction force is then calculated by integrating the pressure over the non-cavitating region. This approach is similar to that of Brindley *et al.* [4], except that they have a different criterion for fixing the pressure at one point (oil inlet) and, of course, they use the lubrication approximation. In our case, fixing the pressure at the point of smallest gap is done so that we can compare results with the π film model and for no other reason. The physical significance of doing this is discussed in our conclusions.

4.3. Comparison between Single and Dual Phase Cavitation Approach

To enhance the comparison we label the three different approaches as such:

- A, the dual-phase π-film cavitation model;
- B, the single-phase π-film cavitation model;
- C, the single-phase variable-film cavitation model.

Although, strictly speaking, the approach A to the cavitation model and approach B are the same cavitation model with different numerical models we shall refer to them as cavitation models.

In qualitative terms there is little difference between any of the three cavitation models. As reported in [3] (cavitation model A) the journal's path is governed, in the lubrication approximation, by the four parameters S, $\overline{\omega}$, ε_0, and ϕ_0, whilst the stability of the path is governed by S and $\overline{\omega}$. The same can be said for the lubrication theory associated with cavitation model B, where the journal's motion, in lubrication theory, is determined by (45) and (46). Both approaches result in paths that fall into one of three stability regimes, namely, equilibrium point, closed path, or unstable path. No lubrication approximation was made with cavitation model C, although we report that this model also produced paths that fell into one of the three stability regimes.

Qualitatively, however, there are significant differences between the three models as we will illustrate by showing the resultant paths for different values of mass M_e, angular velocity ω, and initial position (ε_0, ϕ_0).

We shall only show one example of a path for model B since we acknowledge that it is a very unrealistic model. However, we can deduce useful information regarding the other cavitation models from this model. We illustrate all three paths for our first example (see Fig. 13), with $M_e = 7 \times 10^4$ kg/m, $\omega = 1350$ rad/s which correspond to the dimensionless parameters $(S, \overline{\omega}) \approx (0.0588, 3.818)$. The initial position of the journal is $(\varepsilon_0, \phi_0) = (0.8175, \pi/2)$. The result is that model A displays an unstable path whilst models B and C both display closed paths. The closed path of model B is the most stable of the two since the journal enters the loop in the shortest time and with the least number of whirl rotations. In fact in all of our examples we found model A to give the least stable path with model B giving the most stable.

The fact that model B and model A disagree quantitatively is an indication that the pressure field in a dynamically loaded system is far from anti-symmetric which is the basis for using the π-film cavitation model. In fact if the pressure field was anti-symmetric then the paths of all three models would be identical. It can be argued that model A is more realistic than model B since having made the anti-symmetric assumption this is carried through the whole solution process. Therefore, having highlighted one of the failings of the π-film model we eliminate model B from our discussions and concentrate solely on comparing model A with model C. Model C, of course, only fixes the pressure at one point which is physically viable.

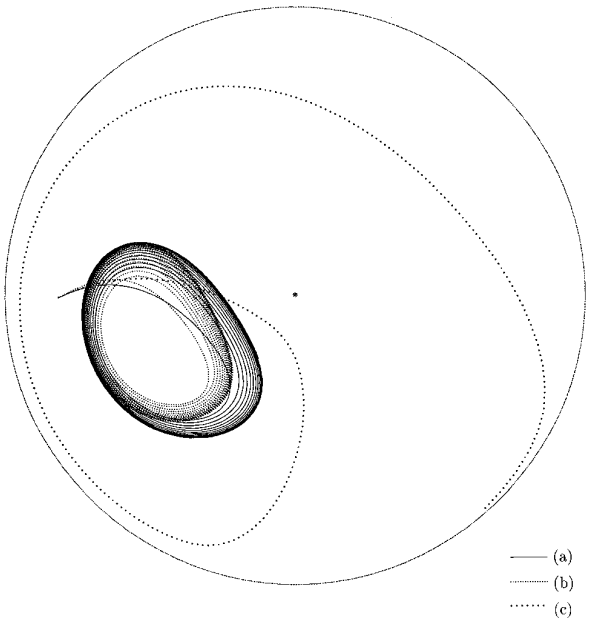

FIG. 13. Comparison of the paths of (a) variable-film single-phase (model C), (b) π-film single-phase (model B), and (c) π-film dual-phase (model A) caviation models for a journal of $M_e = 7 \times 10^4$ kg/m with $\omega = 1350$ rad/s and $(\varepsilon_0, \phi_0) = (0.8175, \pi/2)$ with times (a) $t \in [0, 0.122]$, (b) $t \in [0, 0.170]$, (c) $t \in [0, 0.149]$.

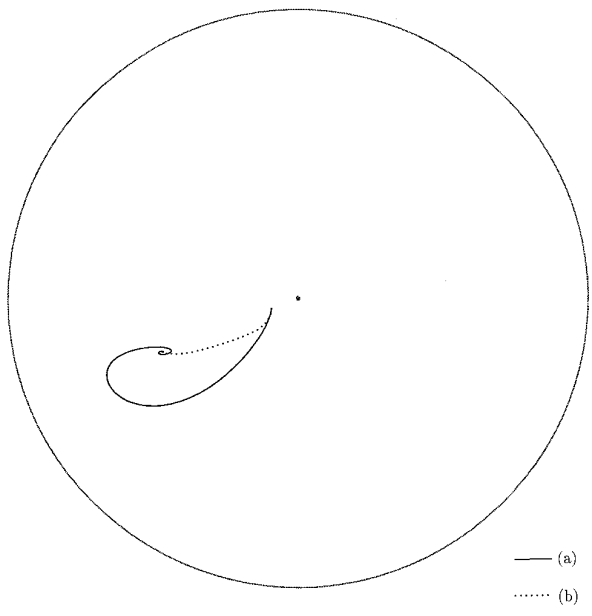

FIG. 14. Comparison of the paths of (a) π-film double-phase (model A) and (b) variable-film single-phase (model C) cavitation models for a journal of $M_e = 1.75 \times 10^4$ kg/m with $\omega = 350$ rad/s and $(\varepsilon_0, \phi_0) = (0.1, 1.22)$ with time $t \in [0, 0.06]$.

Our second example is for a journal of mass per unit length, $M_e = 1.75 \times 10^4$ kg/m and angular velocity $\omega = 350$ rad/s which corresponds to the dimensionless numbers $(S, \overline{\omega}) \approx (0.0607, 0.990)$ and for an initial position of $(\varepsilon_0, \phi_0) = (0.1, 1.22)$. Figure 14 shows the two paths corresponding to cavitation models A and C and it is clear that both paths tend towards the same stable equilibrium point, although the paths are significantly different. The path corresponding to the dual-phase approach has a more "spirally" path which is a far less direct route than that exhibited by the single-phase approach. As expected the equilibrium point of both approaches are the same, that is, $(\varepsilon_f, \phi_f) = (0.5065, 0.3584)$, which compares with the lubrication theory value of (0.5068, 0.3581). As a further illustration of the paths, Figs. 15 and 16 show the variation of the eccentricity and attitude angle of the journal plotted with time. The pressure on the journal for both cavitation models are shown in Figs. 17 (model C) and 18 (model A); each one shown at equal time intervals up to $t = 0.3$ s. It is clear that the maximum pressure peak in the dual-phase model is higher than in the single-phase model but this is due to the higher eccentricities attained in the dual-phase model. The fundamental difference in the two approaches is also clear in these diagrams. The pressure varies significantly throughout the region for model C whilst for model A the low viscosities in the divergent film cause the pressure in that region to be nearly zero. With a squeeze velocity the pressure increases dramatically from the stationary situation. As time progresses the pressure in both cases approaches the pressure distribution for the stationary journal at the equilibrium point and eventually the pressure distribution for the $\theta \in [0, \pi]$ region for both models will agree; at $t = 0.3$s this is not quite the case.

In our third example, the physical parameters of $M_e = 4 \times 10^4$ kg/m, $\omega = 800$ rad/s which correspond to $(S, \overline{\omega}) \approx (0.0609, 2.263)$ result, as expected, in less stable trajectories than in the previous example. The initial position of the journal is $(\varepsilon_0, \phi_0) = (0.825, 1.14)$. Figure 19 shows the two paths corresponding to cavitation models A and C with the double-phase approach resulting in a closed loop, whilst the single-phase approach tends towards the equilibrium point in a spiral fashion. This equilibrium point is, to within four figures, the same as the equilibrium point in

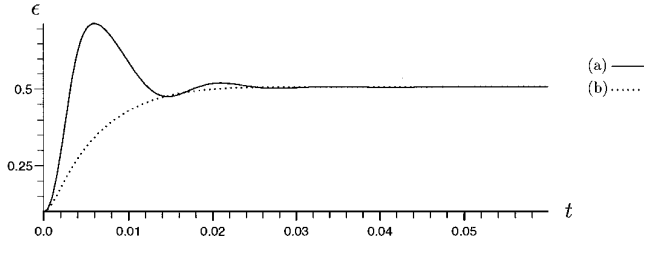

FIG. 15. Plots of (a), (b), the eccentricity of the two journal paths shown in Figs. 14a,b, respectively.

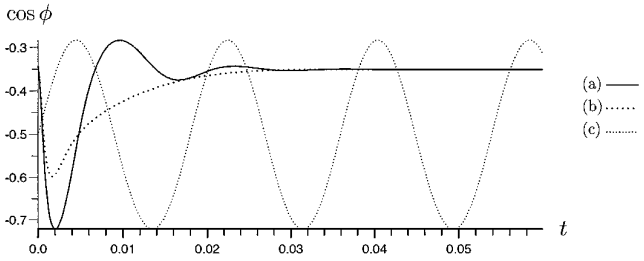

FIG. 16. Plots of (a), (b), the cosine of the attitude angle of the journal paths shown in Figs. 25a,b respectively, together with (c) $k_1 + k_2 \sin(\omega t)$ for reference with the journal's angular velocity.

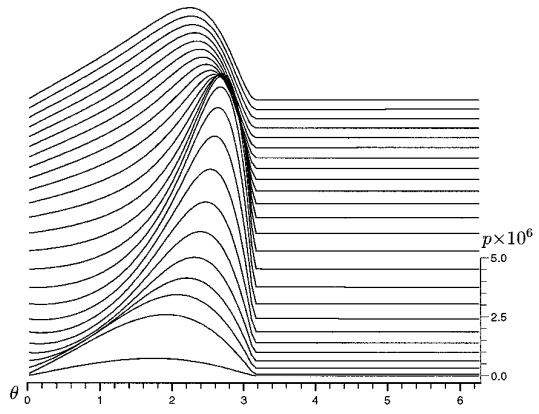

FIG. 18. The pressure distribution on the journal for the dual-phase π-film (model A) example illustrated in Fig. 14, measured at equal time intervals up to $t = 0.3$.

the previous example which again supports the conjecture that for the lubrication approximation the equilibrium point is a function of the Sommerfeld number. Due to the maximum eccentricity, $\varepsilon_{\max}$, of the double-phase approach being approximately 0.98 a finer spatial discretisation grid of $(E_r, E_a, N_r, N_a) = (8, 12, 1, 4)$ is used for this example. Figures 20 and 21 compare the eccentricities and attitude angles of the two approaches. We note that the whirl speed of the closed path is not half the angular velocity of the journal, which is contrary to the claims made in [3]. The calculated value is 0.731ω.

Our final example (Figs. 22, 23, and 24) in this section is for $M_e = 7 \times 10^4$ kg/m, $\omega = 1500$ rad/s, corresponding to $(S, \overline{\omega}) \approx (0.0650, 4.243)$ for the same initial position as the last example. The resulting paths for both approaches are more unstable than in the previous example with both giving physically unstable paths. The double-phase approach reaches $\varepsilon = 0.98$ at $t = 0.0125$ s, as compared with the previous example's value of $t = 0.014$ s, whilst the single-phase approach is clearly more unstable than in the previous example. Measuring the whirl speed the trajectories for this example would be almost meaningless since, again, an approximately closed path has not been reached.

We know that for a zero applied load system that a physically unstable dual-phase π-film model will tend, with time, towards the half-speed case. Whether this is the case for a constant applied load we do not know, although with the variable applied load, mentioned later, this does seem visually to be the case. The numerical calculation of whirl speed for limiting cases of the eccentricity is very difficult and is, to be honest, of little interest to engineers since it occurs at eccentricities far higher than the onset of bearing failure. We note, however, that we have shown that there exist closed loops with constant applied load which have a whirl speed that is not half-speed.

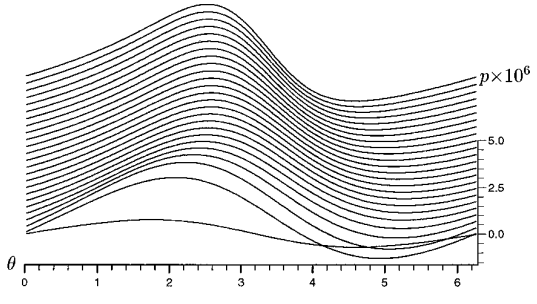

FIG. 17. The pressure distribution on the journal for the single-phase variable-film (model C) example illustrated in Fig. 14, measured at equal time intervals up to $t = 0.3$.

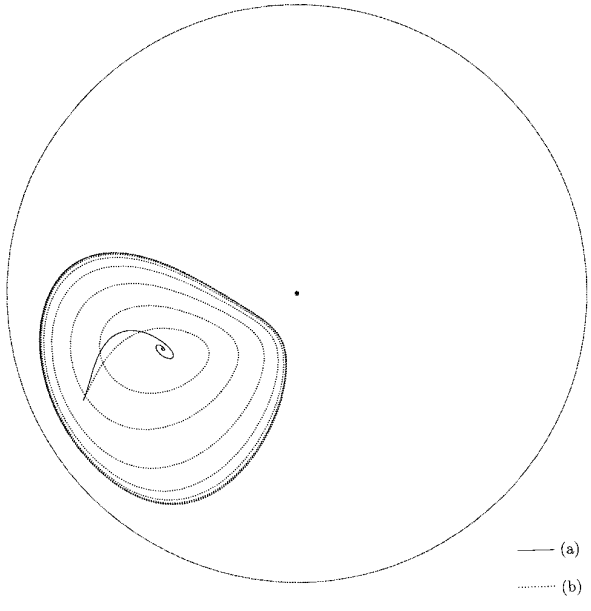

FIG. 19. Comparison of the paths of (a) variable-film single-phase (model C) and (b) π-film double-phase (model A) cavitation models for a journal of $M_e = 4 \times 10^4$ kg/m with $\omega = 800$ rad/s and $(\varepsilon_0, \phi_0) = (0.825, 1.14)$ with time $t \in [0, 0.1]$.

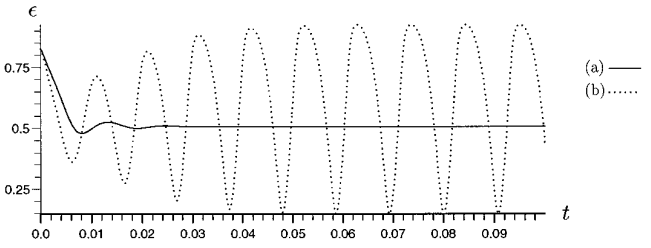

FIG. 20. Plot of the eccentricity of the journal's paths shown in Fig. 19.

Remarks. The π-film cavitation model used in [3] has, as its justification, the results of statically loaded journal bearings where the pressure field is anti-symmetric, up to an arbitrary pressure constant, along the line joining the centres of the bearing and the journal. We have shown that the assumption of anti-symmetry should not be made for dynamically loaded journal bearings. However, the π-film cavitation model is still employed, in journal bearing calculations. This model has been widely reported to be unrealistic, although we are unaware of papers that quantify to which extent that this model is in error. What we have done is to take two different approaches to the π-film cavitation model, which, if the anti-symmetry property was realistic then their paths would agree. Since their paths are clearly quantitatively different then the π-film cavitation model must be unsuitable for dynamically loaded journal bearings.

Keeping with the assumption that the pressure is ambient on the journal at the point of smallest gap and that subambient pressures cavitate we have employed a more realistic model which employs the single-phase approach (model C). A comparison between this approach and the π-film dual-phase approach shows that the former model gives more stable paths. Having said that we are currently unaware of the effects that the single-phase model has on the paths of the journal. The fact that the π-film model produced significantly different results for the single and dual-phase approaches cannot be used as an indication since the assumptions about the model were erroneous

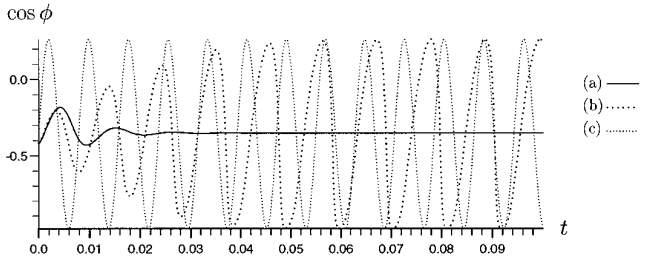

FIG. 21. Plot of the cosine of the attitude angle of the journal paths shown in Fig. 19, together with (c) $k_1 + k_2 \sin(\omega t)$ for reference with the journal's angular velocity.

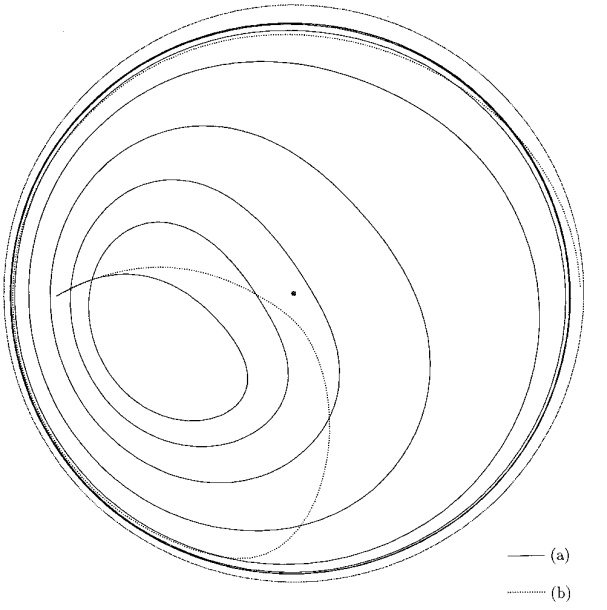

FIG. 22. Comparison of the paths of the (a) variable-film single-phase (model C) and (b) dual-phase π-film (model A) cavitation models for a journal of $M_c = 7 \times 10^4$ kg/m with $\omega = 1500$ rad/s and $(\varepsilon_0, \phi_0) = (0.8175, \pi/2)$ with time (a) $t \in [0, 0.0902]$,(b) $t \in [0, 0.0125]$.

which might well have amplified the differences. Our next step is to employ a dual-phase variable-cavitation model and to compare the results with the single-phase model. This approach is not numerically trivial since, unlike, model A, the cavitation boundary need not lie on an elemental interface. This new dual-phase approach involves the solution of the fluid equations twice at each time step; stage 1 solves the problem for the full-film to find out where the subambient pressures occur and stage 2 solves the problem with the cavitation region being a fluid of low viscosity. The assumption is made that the cavitating region will be the region giving subambient pressures in the full film case. The nontrivial numerical difficulty of viscosity discontinuities will be overcome by employing a C^∞ viscosity function, similar to that presented in [7], across the region of discontinuity.

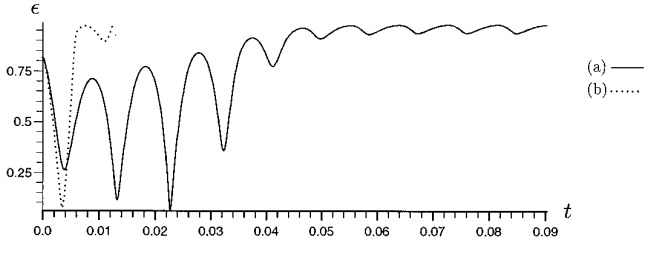

FIG. 23. Plots of (a), (b), the eccentricity of the two journal paths shown in Figs. 22a,b, respectively.

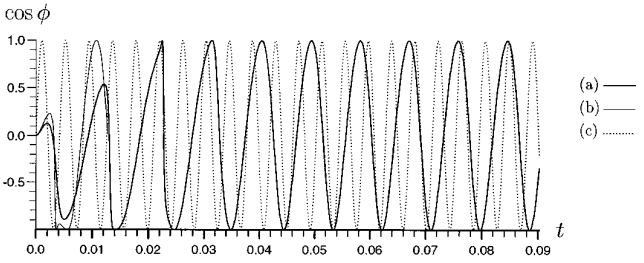

FIG. 24. Plots of (a), (b), the cosine of the attitude angle of the journal paths shown in Figs. 22a,b, respectively, together with (c) $k_1 + k_2 \sin(\omega t)$ for reference with the journal's angular velocity.

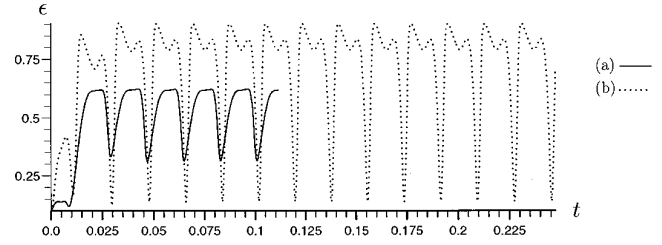

FIG. 26. Plots of (a), (b), the eccentricity of the two journal paths shown in Figs. 25a,b, respectively.

5. VARIABLE LOAD PREDICTIONS

In the following section we investigate the effect of a variable load on the journal's path. Thus we have a nonzero F_p in Eq. (33). Variable applied loads were not considered by Brindley *et al.* [3] but it is a simple matter to include them into the equations of motion presented in that paper. The lubrication theory agreed well with the fully nonlinear results and, hence, we will concentrate on making comments on the resulting paths.

For the case of the full film condition no change in the end effect of the journal's path was found; that is, the journal always tended towards the bearing. The initial path would be changed by the variable load but as time passed the path would progressively resemble, to the eye, the half-speed whirl.

When cavitation was included we found that physically stable systems (stable equilibrium point) under $F_p = 0$ sometimes resulted in closed paths when acted upon by a variable applied load ($F_p \neq 0$). The whirl speed of the resulting closed paths was the same as the period of the variable applied load. Although this indicates that the variable applied load is the dominant forcing term this is not necessarily the case as we shall demonstrate with an example. Figure 25 shows the comparison of the paths resulting from the two cavitation models A and C with a variable applied load given by $F_p = 2 \times 10^5$ N/m, whilst all the other physical parameters are the same as the stable equilibrium paths shown in Fig. 14. Fig. 26 shows the corresponding evolution of the eccentricity ratio. Two different closed paths result, whilst a study of the whirl speed, from Fig. 27 shows that the period of the paths are the same as the period of the variable applied load ($2\pi/\omega$ s). Figures 28 and 29 show the comparison of the fluid reaction forces of the two cavitation models (C) and (A), respectively, with the variable applied load. In actual fact, the x and $-y$ components of the reaction force are shown, $(R_x, -R_y)$, the latter so as to ease comparison with the applied load. Recall that the applied load is applied in the vertical direction. Figure 29 clearly shows that the reaction force corresponding to the single-phase model does seem to be a reaction to the applied load in the sense that the x-compo-

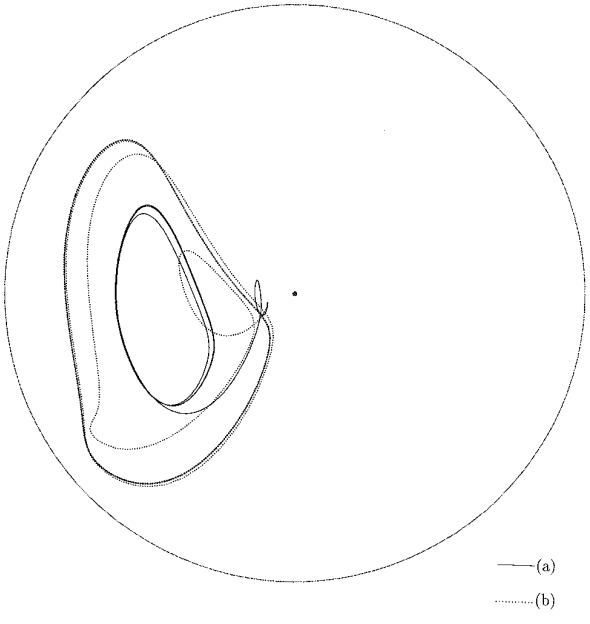

FIG. 25. Comparison of the paths of (a) variable-film single-phase and (b) π-film double-phase cavitation models for a journal of $M_e = 1.75 \times 10^4$ kg/m, $\omega = 350$ rad/s, $(\varepsilon_0, \phi_0) = (0.10, 1.22)$, $F_p = 2 \times 10^5$ N/m, $F_c = 0$ N/m with time $t \in$ (a) [0, 0.11], (b) [0, 0.25].

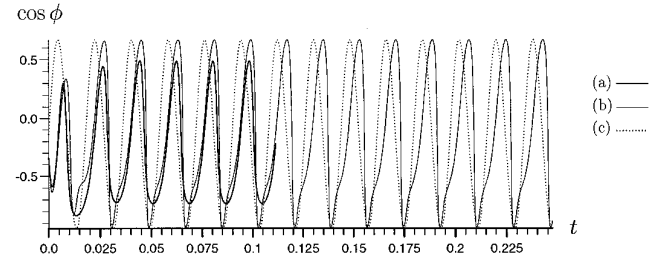

FIG. 27. Plots of (a), (b) the cosine of the attitude angle of the journal paths shown in Figs. 25a,b, respectively, together with (c) $k_1 + k_2 \sin(\omega t)$ for reference with the journal's angular velocity.

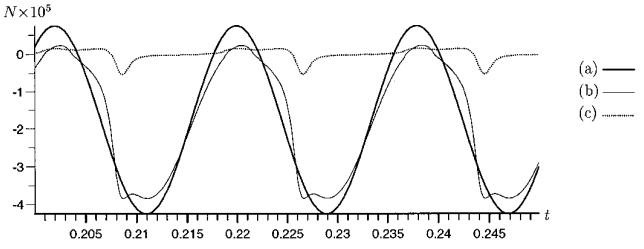

FIG. 28. Plot of the forces on the journal for the cavitation model C for the path illustrated in Fig. 25a for $t \in [0.2, 0.35]$ with (a) applied load F, (b) $-R_y$, and (c) R_x.

nent of force is small, whilst the y-component is approximately equal and opposite to the applied load. Having shown the reactive nature of the fluid's force on the journal for this cavitation model it is not surprising that they (i) have an effect on the journal's path and (ii) they are of the same period as the driving force. Much less predictable results derive from the dual-phase π-film model as shown in Fig. 29. In the region in which the applied load is quite small the behaviour of the reaction force is reasonably predictable; that is, a small x component and a y-component roughly equal and opposite to the applied load. However, when the applied load becomes large in magnitude the reaction force demonstrates an unusual behaviour with the x component becoming significant and the y-component showing a double peak.

We believe that this behaviour is due to the implementation of the dual-phase approach in the cavitation model as opposed to the assumption of π-film cavitation. Admittedly this belief is based solely upon the result of running cavitation model B (single-phase π-film) for the same problem and discovering that the behaviour of the reaction force was very much akin to the behaviour found with cavitation model C. We do not pursue the case further in this paper except that we note that such differences between the cavitation models in the force could well be an indication, when compared with experimental results, as to which numerical approach is the more realistic.

In all of our runs with variable applied loads of whatever magnitude, the fluid's reaction force was comparable, in magnitude, with the applied load and, hence, the choice of cavitation model became important in calculating the journal's locus.

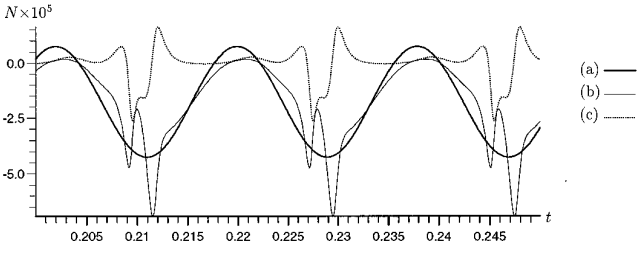

FIG. 29. Plot of the forces on the journal for the cavitation model A for the path illustrated in Fig. 25b for $t \in [0.2, 0.35]$ with (a) applied load F, (b) $-R_y$, and (c) R_x.

We cannot comment whether the application of a non-zero F_p to a previously stable system always produces a closed path. Unsurprisingly there always exists a large enough F_p for which the eccentricity ratio of the journal eventually exceeds our permitted value of $\varepsilon = 0.98$, although there may well be, theoretically, a resultant closed loop if this restriction were not imposed.

Finally, we discuss the results of the numerical algorithm using parameters which, on the face of it, are physically realistic. We know that the force parameters $F_p = 2500$ N/m and $F_c = 0$ N/m are realistic values for the force generated by the crankshaft in a car engine [17]. The *actual* mass per unit length of a crankshaft (journal), that is, its mass per unit length when removed from the rest of the engine, is of the order of 50 kg/m. The result of using the above force values and setting M_e to be its *actual* mass of 50 kg/m results in paths with properties quite unlike those found in the car engine. For the cavitation model A the journal enters an almost half-whirl motion with a very slowly increasing average eccentricity eventually leading to bearing failure. The applied load had only a very small effect on the journal's path. Under cavitation model B the resultant path was a very small closed loop in the close neighbourhood of the bearing's centre. Neither of these results are physically realistic from experimental studies of the journal bearing problem in which closed paths exist with high variations in eccentricity [2]. We believe that this is attributable to the limitations of the long bearing approximation.

6. CONCLUDING REMARKS

A detailed study of the nonlinear dynamics of journal bearings has been made by Brindley *et al.* [5] and, whilst we cannot compare our results with those found in that paper since they investigated the short bearing, they do express a requirement for a more realistic journal bearing model than found in their work. We have described here the basics of our algorithm which has the capability of modelling such physical properties as a variable applied load and non-Newtonian effects which can be extended to include viscoelasticity. For the case of a Newtonian fluid and large journal angular velocity we find that the quasi-steady algorithm is sufficient to calculate the journal's motion and we validate our numerical model for the Newtonian fluid by comparing some results with those of [3].

With a constant applied load and π-film cavitation we find the existence of a closed path whose period is not that of half-speed. Previous papers only report the existence of half-speed closed orbits. We have illustrated the exis-

tence of closed loops under a varying applied load which, despite having a period the same as the applied load, have paths which are sensitive to the cavitation model used. This indicates that the period of the path is by no means an indication of what the dominant driving forces are. Even for large magnitude applied loads the choice of the cavitation model is important.

To compare with experimental observations the problem of calculating the effective mass M_e must be addressed. This may well be much bigger than the actual mass of the crankshaft. To take into account engine friction forces the effective mass can be time-dependent. An inverse problem approach may be pursued.

Our next objective is to develop a more realistic cavitation model than those mentioned in this paper. The π-film model is shown to be unreliable, whilst in the oscillatory model described in [4] the forces are calculated from results derived from the full-film model. We can take advantage of the flexibility of the numerical algorithm by, for example, setting the pressure volume integral to be zero and then deem all subambient pressures to be cavitating and then rerun the calculations under the assumption of that cavitating region. In [4] the pressure arbitrariness was removed by the assumption that the oil feed is at an ambient pressure. Since we are dealing with the fully nonlinear model in 2-D we are unwilling to introduce this assumption. In this paper we used the assumption that pressure was set on the journal at the smallest gap. The ''zero pressure volume'' model is free of a major failure of the variable-film model, where a dominant squeeze film velocity can generate a full-film cavitating region if the fixed ambient pressure coincides with the region of peak pressure. With the zero pressure volume model the pressure at every point in the fluid is a function of the physics of the model. This, we feel, is certainly true for the 2-D model without oil feed. In the 3-D model things are different since ambient pressures exist at the ends of the journal bearing cylinders. For the ''volume integral'' cavitation model with a rotating statically loaded journal bearing the half-Sommerfeld condition is recovered.

An important next step is to consider the non-Newtonian effects on the journal's locus. A shear thinning viscosity model which, when using viscosity ''cutoff'' as described in [7], gives pressure profiles not dissimilar to the profiles found when implementing π-film cavitation. Whether this viscosity model has a similar stabilising effect as the π-film cavitation model will be very interesting and, if so, which is dominant in realistic journal bearings. Following on further from the variable viscosity effects is the role that viscoelasticity has to play in this puzzle.

This paper also described the NISDAT algorithm and, although all the results produced were generated using the quasi-steady algorithm, they were all checked against the NISDAT results. The differences between the two methods were negligible which is to be expected in the absence of inertia and viscoelasticity. Having validated the NISDAT algorithm for the Stokes fluid we intend to use it in the study of viscoelastic and inertial effects on the journal's path, two examples which the quasi-steady algorithm cannot model. The numerical stability of the NISDAT algorithm needs to be investigated, although preliminary results indicate that problems occur only for journal mass well below physical reality.

ACKNOWLEDGMENTS

This work was funded by Shell Research Ltd., Thornton, UK. We have benefited from collaboration with Drs. T. Bates, R. Coy, L. Scales, and A. Schlijper at Shell Research Ltd. and with Drs. X. K. Li, G. W. Roberts, and Professor K. Walters at the University of Wales.

REFERENCES

1. H. A. Barnes, J. F. Hutton, and K. Walters, *An Introduction to Rheology* (Elsevier, Amsterdam, 1989).
2. T. W. Bates, B. Williamson, J. A. Spearot, and C. K. Murphy, Society of Automotive Engineers, Paper No. 860376, 1986 (unpublished).
3. J. Brindley, L. Elliott, and J. T. McKay, *ASME J. Appl. Mech.* **50,** 877 (Dec. 1983).
4. J. Brindley, L. Elliott, and J. T. McKay, *ASME J. Appl. Mech.* **50,** 886 (Dec. 1983).
5. J. Brindley, M. D. Savage, and C. M. Taylor, *Phil. Trans. Roy. Soc. London A* **332,** 107 (1990).
6. A. Cameron, *Basic Lubrication Theory* (Ellis Horwood, Chichester, 1981).
7. A. R. Davies and X. K. Li, *J. Non-Newtonian Fluid Mech.* **54,** 331 (1994).
8. W. J. Gordon and C. A. Hall, *Int. J. Numer. Methods Eng.* **7,** 461 (1973).
9. D. Rh. Gwynllyw and T. N. Phillips, *SIAM J. Sci. Comput.*, to appear.
10. B. J. Hamrock, *Fundamentals of Fluid Film Lubrication* (McGraw-Hill, New York, 1994).
11. R. Holmes, *Proc. Inst. Mech. Eng.* **177**(ii), 291 (1963).
12. Y. Maday, D. Meiron, A. T. Patera, and E. M. Rønquist, *SIAM J. Sci. Comput.* **14,** 310 (1993).
13. Y. Maday and A. T. Patera, ''Spectral Element Methods for the Incompressible Navier–Stokes Equations, in *State of the Art Surveys in Computational Mechanics* (A. K. Noor and J. T. Oden, Eds.) (ASME, New York, 1989), p. 71.
14. J. R. Mitchell, R. Holmes, and J. Byrne, *Proc. Inst. Mech. Eng.* **180,** 593 (1966).
15. O. Reynolds, *Phil. Trans. Roy. Soc.* **177**(i), 157 (1886).
16. G. W. Roberts and K. Walters, *Rheol. Acta* **31** (1992), 55–62.
17. Correspondence with Shell Ltd, Thornton Research Centre, Cheshire, UK.